Journal of
Synchrotron
Radiation

ISSN 1600-5775

Received 14 June 2013
Accepted 27 August 2013

Measurement of the X-ray mass attenuation coefficients of silver in the 5–20 keV range

M. Tauhidul Islam,[a,b] Lachlan J. Tantau,[a] Nicholas A. Rae,[a] Zwi Barnea,[a] Chanh Q. Tran[c] and Christopher T. Chantler[a]*

[a]School of Physics, University of Melbourne, Australia, [b]School of Chemistry, University of Melbourne, Australia, and [c]School of Physics, La Trobe University, Australia.
*E-mail: chantler@unimelb.edu.au

The X-ray mass attenuation coefficients of silver were measured in the energy range 5–20 keV with an accuracy of 0.01–0.2% on a relative scale down to 5.3 keV, and of 0.09–1.22% on an absolute scale to 5.0 keV. This analysis confirms that with careful choice of foil thickness and careful correction for systematics, especially including harmonic contents at lower energies, the X-ray attenuation of high-Z elements can be measured with high accuracy even at low X-ray energies (<6 keV). This is the first high-accuracy measurement of X-ray mass attenuation coefficients of silver in the low energy range, indicating the possibility of obtaining high-accuracy X-ray absorption fine structure down to the L_1 edge (3.8 keV) of silver. Comparison of results reported here with an earlier data set optimized for higher energies confirms accuracy to within one standard error of each data set collected and analysed using the principles of the X-ray extended-range technique (XERT). Comparison with theory shows a slow divergence towards lower energies in this region away from absorption edges. The methodology developed can be used for the XAFS analysis of compounds and solutions to investigate structural features, bonding and coordination chemistry.

Keywords: high accuracy; XERT; X-ray absorption fine structure; silver.

1. Introduction

The development of theoretical and experimental investigations of the interaction of X-rays with atoms has been a continuing effort (Rehr & Albers, 2000; Joly, 2001; Chantler, 1995, 2009; Pettifer *et al.*, 1999; Machali *et al.*, 1987; Mica *et al.*, 1985; Lytle, 2007). X-ray mass attenuation coefficients $[\mu/\rho]$ and form factors describe the interaction of X-rays with atoms and are widely used. Absolute measurement of $[\mu/\rho]$ is of great interest for testing of atomic theories and for comparison with existing tabulations of $[\mu/\rho]$ in the literature (*e.g.* FFAST and XCOM tabulations). X-ray mass attenuation coefficients are used in medical science to generate X-ray images and computed tomography (Lee *et al.*, 1991). Measurements of X-ray mass attenuation coefficients are also important for the study of bonding and local atomic structure of materials and molecules (Han *et al.*, 2002; Ignatov *et al.*, 2001), of the density of electronic states (Hossain *et al.*, 2005) and to test predictions of the photoabsorption (Gerward *et al.*, 1979; Gerward, 1989; Karabulut *et al.*, 2005) and elastic scattering (Hopersky *et al.*, 2004; Khoperskii *et al.*, 2005) using bound state electron wavefunctions. Recently, nano-roughness measurement of thin foils has also become possible using X-ray mass attenuation data (Glover *et al.*, 2009). Measurements of X-ray mass attenuation coefficients have, therefore, been a subject of great interest of several research groups around the world.

This work measures $[\mu/\rho]$ in the region between the K and L_1 absorption edges of silver and tests the XERT (X-ray extended-range technique) for its suitability for high-accuracy XAFS measurements of such a high-Z element. We also extend measurements of the absorption of silver to lower energies, down to 5 keV, close to its L edge at 3.8 keV. To do this, we tested a number of foils between 5 µm and 100 µm thick for their suitability for accurate measurements at these lower energies. The thinnest 5 µm foil is well suited for accurate measurements at these low energies and will enable us to extend XAFS measurements to the K and L edges using silver foils and silver compounds in solution.

To confirm the high-accuracy in the present measurements, error analysis was performed for experimental systematics relating to dark-current, air-path attenuation, harmonic contamination and energy calibration; statistical reliability is a key question central to the application of XAFS for structural analysis of elements and compounds (Chantler *et al.*, 2012).

2. Experimental

The XERT (Chantler, 2009; Chantler *et al.*, 2001; de Jonge *et al.*, 2006) has been used for the high-accuracy measurement of mass attenuation coefficients of various elements, of form factors and X-ray absorption fine structure (XAFS), and has produced some of the most accurate measurements of mass attenuation coefficients (de Jonge *et al.*, 2005; Glover *et al.*, 2008; Rae *et al.*, 2010; Islam *et al.*, 2010). XERT measurements are performed over an extended range of experimental parameters allowing the determination of sources of systematic errors such as scattering and fluorescence (Tran *et al.*, 2004), harmonic content (Barnea & Mohyla, 1974), energy drift (Glover *et al.*, 2010), bandwidth (de Jonge *et al.*, 2004*a*), dark current and the attenuation by the detectors and by the air path.

Fig. 1 represents a schematic of the experimental set-up at the ANBF, Tsukuba, Japan. In this work, the mass attenuation of silver was measured using an X-ray beam produced by a bending magnet at beamline 20B of the Photon Factory in Tsukuba, Japan. The X-ray beam was monochromated by a double-crystal monochromator using a monolithic silicon 111 crystal located in the first optical enclosure. The monochromated X-rays were passed through a pair of orthogonal adjustable slits for defining the beam cross-section (approximately 2 mm × 1.5 mm).

Matched ion chambers were located upstream and downstream from the attenuating silver foils and were run using a flow of nitrogen gas. The beam intensity was continuously monitored. To achieve high precision, each of the measurements was repeated at least ten times. The monochromator was set to produce photons of energy well above 20 keV and then gradually stepped down to lower energies during the attenuation measurements to avoid effects of backlash.

The sample stage was configured so that it could hold three silver samples and translate and rotate them about horizontal and vertical axes perpendicular to the beam. Two daisy wheels containing 15 aluminium foils each around its perimeter were mounted between the sample stage and the two ion chambers. The aluminium foils had thicknesses varying over several orders of magnitude and allowed us to record additional information about thickness dependence of systematic errors.

2.1. The silver foil samples

A total of seven silver foils with nominal thicknesses ranging from 5 μm to 275 μm were used to measure the X-ray mass attenuation coefficients of the silver foils. The foils were supplied by Goodfellow with claimed purity of 99.99%. The masses and areas of the foils were determined from repeated measurements using a microgram balance and an optical comparator, respectively. The average for each foil was used with a respective standard error determined from the variance of the repeated measurements. Of the two 100 μm foils, the foil in the 15–20 keV energy range (Fig. 4) was used as the reference with a determined mass M = 0.6911 g ± 0.000001 (0.0014%) and area A = 6.493 cm^2 ± 0.0019 (0.03%). The average integrated column density $[\rho t]_{\rm av}$ of the reference foil was found to be $[\rho t]_{\rm av}$ = 0.10644 g cm^{-2} ± 0.00003 (0.03%) from the ratio of the mass M to the area A of the foil. We identify the foils by their nominal thicknesses, but of course only measured values were used in the analysis.

3. Analysis details

3.1. Dark-current analysis

Dark currents were recorded by the ion chambers at each of the energies to correct for its effect on sample attenuations. The dark current is a function of time and has been shown to have significant effect on the attenuation measurements (Glover & Chantler, 2007). For the first time, a stepwise fitting procedure was followed to fit the recorded dark currents at two successive energies with respect to the time difference between the two measurements using a covariance matrix. The fitted dark currents were then subtracted from measurements recorded with and without the foil in both upstream and downstream ion chambers. This new approach to dark-current fitting produced greater consistency and lower χ^2 values, thereby allowing reduction of uncertainty contributions from this particular source of systematic error.

3.2. Determination of integrated column density

The accurate determination of the integrated column density $[\rho t]_{\rm c}$ along the beam path is crucial for the determi-

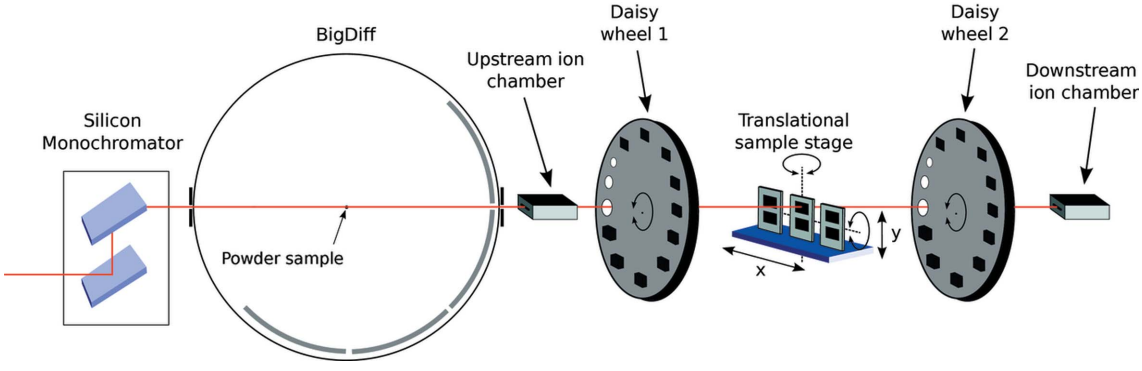

Figure 1
Schematic diagram of the experimental set-up for using the XERT at the ANBF, Tsukuba, Japan. The BigDiff powder diffractometer upstream (to the left) allows energy calibration using standard powder samples. The two daisy wheels (upstream and downstream) monitor harmonic contamination and scattering contributions.

nation of the X-ray mass attenuation coefficients $[\mu/\rho]$. The present analysis used two different methods, *i.e.* full-foil mapping (de Jonge *et al.*, 2004*b*) and 'central-region mapping' (Tran *et al.*, 2003*b*,*c*; Rae *et al.*, 2010) of the foil, to determine the integrated column density $[\rho t]_c$ of the reference foil of nominal 100 µm thickness at the (central) point through which the 2 mm × 1.5 mm X-ray beam passed. The integrated column densities determined by the two methods were consistent. Table 1 and the rest of the paper uses the results of the full-foil mapping technique because of the lower uncertainty in the determined $[\rho t]_c$.

The attenuations across the area of the foil were measured using an X-ray raster scan with the 2 mm × 1.5 mm beam size. The average $[\mu/\rho][\rho t]_{av}$ of the attenuations $[\mu/\rho][\rho t]_i$ across the area and the attenuation at the central point used for all attenuation measurements were determined from the obtained attenuation map of the foil. This followed the modelling of the foil and a fitting procedure applied to the experimental data. The mass m and area A of the foil were used to determine the average integrated column density $[\rho t]_{av}$. Finally, the information was used in equation (1) to determine the integrated column density $[\rho t]_c$ and the corresponding uncertainty of the reference foil,

$$[\rho t]_c = \frac{[\mu/\rho][\rho t]_c}{[\mu/\rho][\rho t]_{av}}\,[\rho t]_{av},$$
$$\sigma_{[\rho t]_c} = \left[\left(\frac{\sigma_{[\mu t]_c}}{[\mu t]_c}\right)^2 + \left(\frac{\sigma_{[\mu t]_{av}}}{[\mu t]_{av}}\right)^2 + \left(\frac{\sigma_{[\rho t]_{av}}}{[\rho t]_{av}}\right)^2\right]^{1/2}. \quad (1)$$

3.3. Modelling of the foil and removing the effect of the attenuation of the sample holder

To mount each of the silver foils, a Perspex sample holder was used which also attenuated the X-ray beam (Fig. 2). The average attenuation of the foil was obtained following the subtraction of the attenuation of the Perspex holder used for mounting the foil. In order to remove the effect of the attenuation of the holder, a model of the attenuation of the foil and holder was constructed and fitted to the experimental data (Fig. 3). A square-shaped foil was modelled with two parameters (x_0, y_0) as the central position where x and y describe its axes. The model was then fitted to the experimental data of X-ray attenuations across the entire area of the reference foil. The raster scan mapped the foil completely in both x and y directions. The thickness profile of the modelled

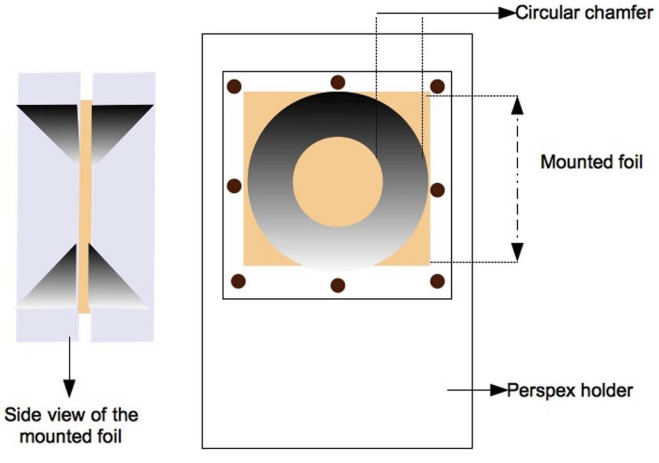

Figure 2
Model of the sample holder. The Perspex transmission must be removed to reveal the map of the foil.

Table 1
Integrated column density $[\rho t]_c$ of reference foils of nominal thickness t_{nom}.

Integrated column density of the reference foil was determined to be 0.108067 ± 0.000101(0.09%) using equation (1). Integrated column densities $[\rho t]$ of the foils were fitted implementing the Levenberg Marquardt algorithm [equation (3)]. Several foils (100 µm, 10 µm, 50 µm and 5 µm foils) were fitted separately to correct for the effect of hysteresis due to multiple measurements and a non-monotonic cycling at 16.5 keV and 16 keV. There were two separate 100 µm foils [100 (1) and 100 (2)], and fitted results prior to hysteresis are labelled (*a*) while results after the hysteretic loop are labelled (*b*). The uncertainties of the column densities were determined by multiplying $(\chi_r^2)^{1/2}$ with the fitted standard errors. χ_r^2 was large at this stage of analysis due to significant roughness and harmonic systematics, which are corrected and optimized as discussed in the text.

t_{nom} (µm)	Fitted values $[\rho t]_c$ (g cm^{-2})	Energy range (keV)
275	0.29221 ± 0.00106	17.00–20.00
100 (1*a*)	0.10813 ± 0.00031	17.00–20.00
100 (1*b*)	0.10740 ± 0.00074	16.00–16.50
100 (2)	0.10639 ± 0.00048	15.00–17.00
50*a*	0.05313 ± 0.00012	17.00–20.00
50*b*	0.05325 ± 0.00027	13.40–16.50
12	0.01328 ± 0.00007	5.00–17.00
10*a*	0.01137 ± 0.00009	16.00–17.00
10*b*	0.01133 ± 0.00006	5.00–16.50
5*a*	0.00501 ± 0.00004	15.00–16.50
5*b*	0.00503 ± 0.00003	5.00–16.00

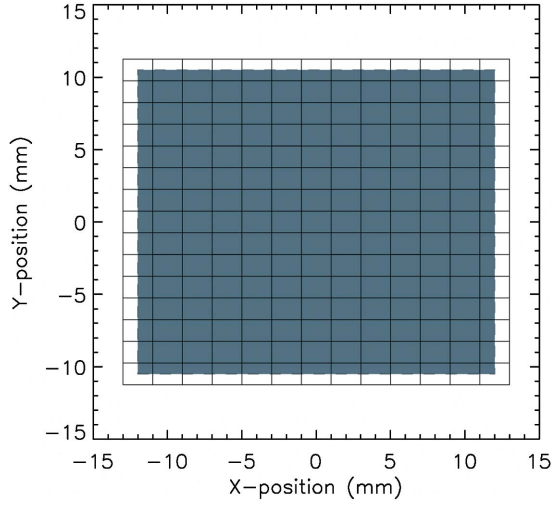

Figure 3
Model of the 100 µm-thick reference silver foil. The blue-shaded square shows the area of the foil over which the X-ray raster scan was performed and the small rectangular grids represent the size and footprint of the X-ray beam for the attenuation measurements of the full-foil mapping.

foil was considered to have the attenuation of a truncated wedge-shaped foil described by Glover *et al.* (2010),

$$[\mu/\rho][\rho t]_{\text{modelled}_{\text{foil}}} = [\mu/\rho][\rho t]_0 + m_x(x - x_0) + m_y(y - y_0), \quad (2)$$

where $[\mu/\rho][\rho t]_0$ represents the attenuation at the central point (x_0, y_0) of the foil. The gradients of the wedge in the x and y directions are represented by the parameters m_x and m_y.

3.4. Determining the average and central-point attenuations, and uncertainties

The attenuation of the well defined holder was then subtracted from the fitted data to obtain the attenuation of the foil (Fig. 4). For the accurate determination of the average attenuation of the foil, the average of all individual attenuations across the scanned portion of the foil was determined. Details of the procedure are described by Glover *et al.* (2010). The standard error determined from the measurements across the foil was taken as the uncertainty of the average attenuation $[\mu/\rho][\rho t]_{\text{av}}$.

3.4.1. The central point attenuation and uncertainty. The area scan of the reference foil (100 µm) was performed with single-point measurements at 17 keV.

The central point attenuation of the reference foil incorporated information of repeated measurements of the central point together with the single-point measurements over the full-foil map,

$$[\mu/\rho][\rho t]_{\text{c}} = \left(\sum_N [\mu/\rho][\rho t]\right)/N.$$

The central-point attenuation was obtained to be 3.039249 ± 0.000278. The average attenuation $[\mu/\rho][\rho t]_{\text{av}}$ was determined from the average of all measurements across the area map shown in Fig. 4, and found to be 2.993479 ± 0.002679. The obtained average and central-point attenuations were then used to determine the absolute integrated column density $[\rho t]_{\text{c}}$ of the reference foil along the beam.

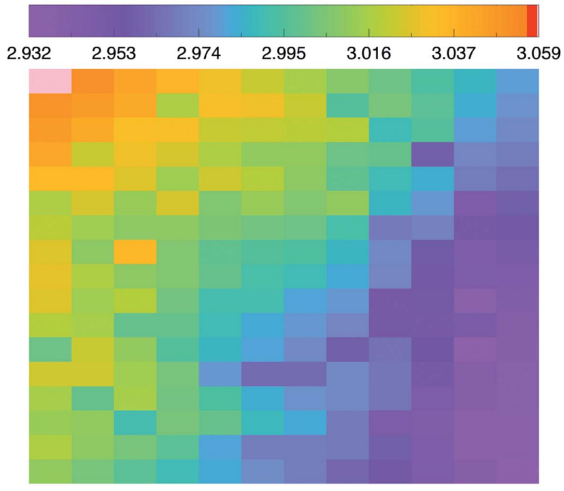

Figure 4
Measured attenuation of the foil after subtraction of the modelled attenuation of the sample holder from the fitted full-foil attenuation. The pixels across the map represent the X-ray beam size of 2 mm × 1.5 mm and the colours indicate small thickness variations inevitable in all foils.

3.5. Determining the integrated column densities $[\rho t]_{\text{c}}$ of the foils relative to the reference foil

A total of seven silver foils were used including the reference foil for the measurements. The full-foil map of the reference foil was used to determine the column densities $[\rho t]$ of the other foils using a fitting procedure.

A hysteretic effect occurred due to a non-monotonic energy cycling. Therefore, we fitted the foils before and after the hysteretic loop. Hence a total of 11 foils were fitted. For instance, the 50 µm foil was fitted over two independent ranges applied at energies before and after 16.5 keV. Similarly, the 10 µm and 12 µm foils were divided into multiple thicknesses to correct for the hysteresis effect across repeated energies 16.5 keV and 16 keV. This approach improved consistency between the weighted mean $[\mu/\rho]_{\text{wm}}$ and the individual measurements $[\mu/\rho]_{\text{i}}$ of the foils using two aperture sizes.

The local consistency between the $[\mu/\rho]$ of different foils and the result with the full-foil mapping is maintained to minimize χ^2 following

$$\chi^2 = \sum_{E_{\text{i}}}\sum_{S_{\text{i}}}\left(\frac{[\mu/\rho]_{E_{\text{i}},S_{\text{i}}} - [\mu/\rho]_{\text{wm}}}{\sigma_{[\mu/\rho]_{E_{\text{i}},S_{\text{i}}}}}\right)^2, \quad (3)$$

where $[\mu/\rho]_{E_{\text{i}},S_{\text{i}}}$ is the mass attenuation coefficient of the sample S_{i} at energy E_{i} with the associated uncertainty $\sigma_{[\mu/\rho]_{E_{\text{i}},S_{\text{i}}}}$, and $[\mu/\rho]_{\text{wm}}$ is the weighted mean of $[\mu/\rho]_{E_{\text{i}},S_{\text{i}}}$ of all foils and aperture-dependent measurements at that energy.

3.6. Determining X-ray attenuation

X-ray intensities were recorded using an upstream (u) and a downstream (d) ion chamber with a sample placed in the path of the X-ray beam, without a sample, and shuttering the X-ray beam for dark-current measurements. Intensities without a sample in the path of the X-ray beam (blank measurements) were also recorded to characterize the air-path attenuation for the X-ray beam travelling the path between the ion chambers. X-ray intensities recorded with the sample, without the sample and the dark current were then used to determine the accurate X-ray attenuation of the sample.

Recorded intensities with the sample and without sample were normalized by subtracting the recorded dark current at each of the energies and used for determining the X-ray beam intensity for both samples and blanks (as a function of energy). The procedure of dark-current fitting and subtraction is discussed in §3.1. The Beer–Lambert law was used for measuring the foil attenuation,

$$[\mu/\rho][\rho t] = -\ln\left[\overline{\left(\frac{I_{\text{d}} - D_{\text{d}}}{I_{\text{u}} - D_{\text{u}}}\right)_{\text{s}}} \Big/ \overline{\left(\frac{I_{\text{d}} - D_{\text{d}}}{I_{\text{u}} - D_{\text{u}}}\right)_{\text{b}}}\right], \quad (4)$$

where the subscripts s and b refer to the intensities measured with a sample in the path of the beam and without any sample

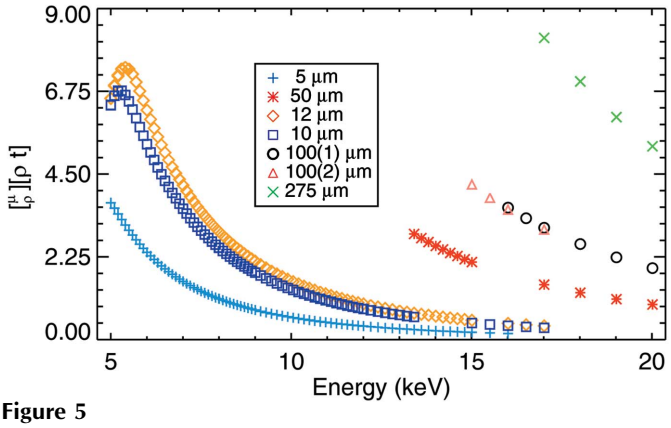

Figure 5
Attenuations of seven silver foils with nominal thicknesses ranging from 5 μm to 275 μm, using equation (4), *versus* nominal monochromator energy. At least three measurements using different thicknesses of foils were made at each energy. Measurements using all the foils were made at 17 keV where the area raster scan of the reference foil (100 μm thick) was made. The attenuation of the various sample thicknesses are represented by the different symbols as indicated.

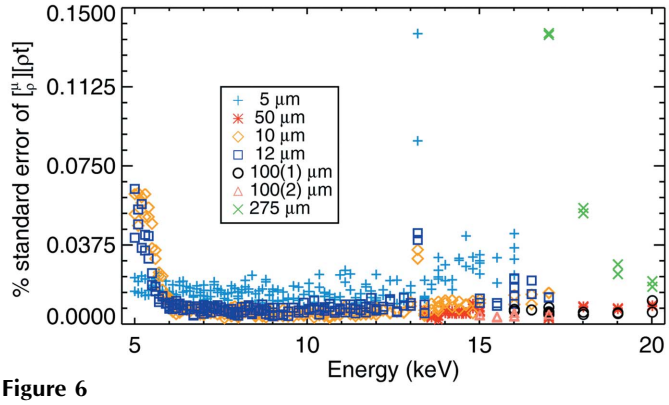

Figure 6
Percentage uncertainties (standard errors) of the foil attenuations *versus* nominal monochromator energy. Uncertainties typically varied from 0.002% to 0.14% where the larger uncertainties were contributed by the thickest foil of 275 μm used in the 17–20 keV energy range. The uncertainties of the attenuations of the other foils were no larger than 0.05% in the 6–17 keV energy range except at 13 keV reaching up to 0.14% due to beam clipping at that point. With the 10 μm- and 12 μm-thick foils, the uncertainties were relatively high at energies below 6 keV.

in the path, respectively. The foil attenuations as a function of energy are shown in Fig. 5.

The uncertainty of attenuation measurements was determined from the uncertainty contributions from dark-current measurements and from the intensities with and without a sample. A total of ten repeated measurements were made for each type of measurement (*i.e.* dark current, blank and sample measurements). The standard errors of the repeated measurements were used to determine the final uncertainty of the attenuation. Thus, the total uncertainty $\sigma_{[\mu/\rho][\rho t]}$ of foil attenuations $[\mu/\rho][\rho t]$ was determined as

$$\sigma_{[\mu/\rho][\rho t]} = \left[\left(\frac{\sigma_{I_{dc}}}{I_{dc}}\right)^2 + \left(\frac{\sigma_{(I_u/I_d)}}{(I_u/I_d)}\right)_s^2 + \left(\frac{\sigma_{(I_u/I_d)}}{I_u/I_d}\right)_b^2\right]^{1/2}, \quad (5)$$

where I_{dc} represents the dark current (*i.e.* recorded intensity when there is no X-ray beam), and the subscripts s and b denote the measurements with a sample in the beam and without a sample in the beam, respectively. The corresponding uncertainties of the foil attenuation are shown in Fig. 6 using the same symbols as in Fig. 5 to represent attenuations for foils of different thicknesses.

3.7. Energy calibration

A key experimental systematic is the energy offset functional caused by the overall hysteresis of the monochromator motor control, which contributes error to the recorded encoder angle of the monochromator (Tantau *et al.*, 2013). This is generically true for all motor or monochromator systems and should be characterized regularly. We used a powder diffractometer to measure directly the energies at which the mass attenuation coefficients of silver were measured, which is much more reliable than encoder settings and currently much more reliable than using an uncalibrated standard foil edge of indeterminate thickness. Two NIST powder standards, Si(640b) and LaB_6(660), were used, the most accurate standards described in the literature. Energy measurements were carried out at every 1–2 keV covering the range of the energies where the attenuation measurements were performed. Detailed energy measurements have been reported by Rae *et al.* (2006). Figs. 7 and 8 show the difference between nominal and calibrated energies and the associated uncertainties of interpolated energies.

A least-squares procedure was performed to fit the differences between the nominal and calibrated energies. For determining the calibrated energy of every attenuation measurement, the best-fit parameters were used. The uncertainties of the interpolated energies were less than 0.62 eV.

4. Effect of harmonic contamination, roughness and their corrections

A 0.01–30% harmonic contamination was observed at lower energies from 8 keV down to 5 keV, which is the highest harmonic contamination observed by our group. This large higher-order harmonic contamination required special treatment for its correction. We investigated two methodologies to determine the contribution of harmonic contamination as harmonic fraction. The 'sample method' used the attenuations of the three main silver foils in the regions of harmonic contamination (10 μm, 12 μm and 5 μm), while the 'daisy-wheel method' used 14 aluminium foils with different thicknesses as mounted on the daisy wheel for harmonic and scattering signatures. Both methods found similar levels of contamination across the range of energies to within a few standard deviations. However, the 'sample method' underestimated the correction, in part because of the sparse information with only three data points per energy. The daisy-wheel method, however, slightly overestimated the harmonic correction, despite a large number of independent measurements (14), in part due to the mismatch between sample and foil attenuation and the different location. Therefore, we investigated the pattern of discrepancies across the range

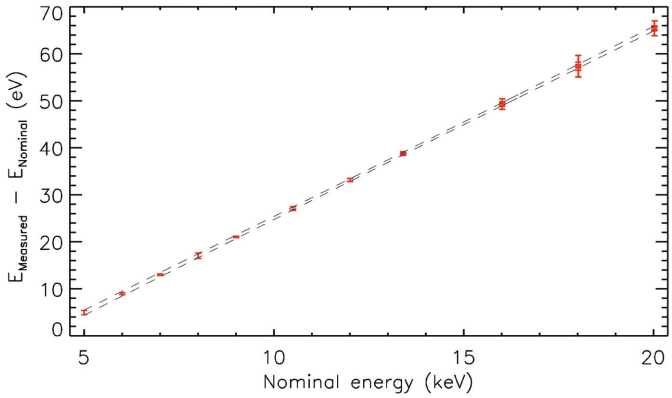

Figure 7
Plot of the difference between the calibrated X-ray energy and the nominal X-ray energy. The calibrated energies were determined using powder diffraction measurements performed on two standard powders, silicon and LaB_6 (red error bars for specific points). Below 11 keV only the LaB_6 powder diffraction patterns produced useful results. The known lattice parameter of the silicon standard and its ratio to the LaB_6 standard were used to determine the energies of the beam. A linear interpolation was then applied to obtain all the energies at which the X-ray mass attenuation coefficients of silver were measured (dashed lines show one standard error upper and lower limits).

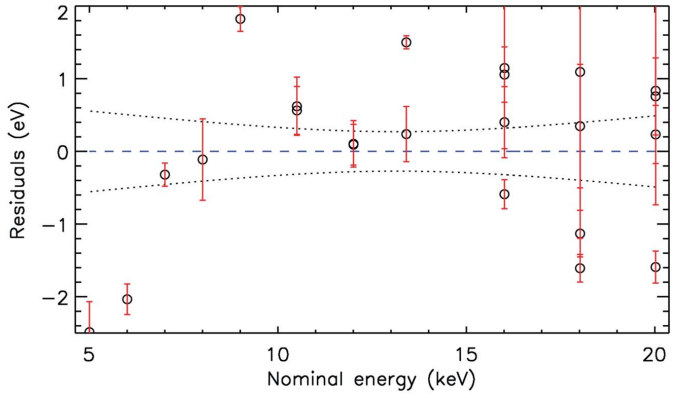

Figure 8
The standard error δE represents the uncertainties of the interpolated measured energies. A covariance matrix was used to determine the variances.

between these estimates in order to minimize the variance. Several patterns were investigated; the optimum fit to the full data set was found using 0.808 times the estimated harmonic fraction from the daisy-wheel method. This approach achieved 0.09–1.22% accuracy in $[\mu/\rho]$ across the full range of energies and samples, and is reported in this paper. We note that there is obviously a residual systematic variance associated with this harmonic, which is dominated at the lowest three measured energies where the correction and its uncertainty are greatest; as such, the residual variance correctly estimates the uncertainty of the corrections in those regions.

4.1. Harmonic contamination and correction

When a monochromator is set to select a particular energy of X-rays, higher-order reflections may also contribute harmonic components to the incident X-ray beam (Tran *et al.*, 2003*a*; Barnea & Mohyla, 1974). These harmonic components were characterized at each of the energies where sample attenuations were measured using a set of aluminium filters. An upstream daisy wheel was used in the experimental set-up to measure the attenuations of 15 aluminium foils mounted around the perimeter of the daisy wheel with thicknesses ranging from 10 µm to 4000 µm. Harmonic components were detected at energies lower than 6.5 keV (Fig. 9).

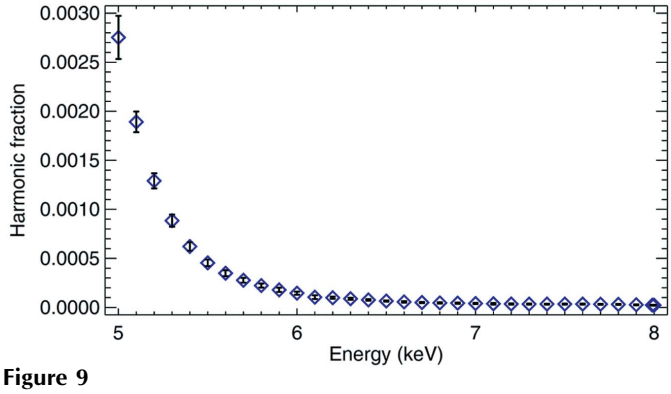

Figure 9
Fractional harmonic contributions at each of the energies at which the X-ray mass attenuation coefficients of silver were measured, based on the daisy-wheel method as discussed in the text. Clearly, the effect of harmonic contamination is noticeable at about 7 keV and increases with decreasing energy.

We used the FFAST tabulated X-ray mass attenuation coefficients of aluminium to characterize and correct for the effect of harmonic components in the X-ray beam. In the presence of harmonic components of energy E_n, the total transmission probability I/I_0 equals the sum of the transmission probabilities for each of the energy components $\exp(-[\mu/\rho]_{E_n}[\rho t])$ weighted by the relative intensity of each component in the incident beam and the relative detection efficiency for each energy component. If a fundamental energy E_1 is contaminated by only one harmonic component of energy E_n, the measured attenuation is given by

$$\exp\{-[\mu/\rho][\rho t]\} = (1 - f_n)\exp\{-[\mu/\rho]_{E_1}[\rho t]\} + f_n \exp\{-[\mu/\rho]_{E_n}[\rho t]\}, \quad (6)$$

where f_n is the fraction of the harmonic component of energy E_n present in the fundamental energy.

4.1.1. Fitting procedure and correction. With the use of this model, we fitted five parameters (harmonic fraction f_n; attenuation $[\mu/\rho][\rho t]_{E_1}$ for fundamental energy E_1; attenuation $[\mu/\rho][\rho t]_{E_3}$ for the third-order energy E_3; a dark current correction; and an offset) to obtain the harmonic effect on the measurements. To obtain the best fit with the lowest χ_r^2, the $[\mu/\rho][\rho t]_{E_3}$ parameter was constrained to the FFAST tabulated values at higher energies and was free at lower energies, while the critical output $[\mu/\rho][\rho t]_{E_1}$ was free for all energies. The dark-current correction and offset were consistent with zero. Following this procedure, harmonic contamination was found to be smooth and monotonic at lower energies <7 keV whereas at higher energies no harmonic contamination was detected. At 5 keV, the obtained harmonic fraction was f_n =

0.0029 ± 0.00011; the attenuation coefficient for the fundamental energy was $[\mu/\rho][\rho t]_{E_1}$ and $(\chi_r^2)^{1/2}$ was found to be 0.0512 at 5 keV. The highest contribution was found at 5 keV (0.29%). The harmonic effect on the attenuations of silver foil was then corrected for making use of the fractional harmonic contribution at each of the energies by reversing equation (6). This subtracts the attenuation for the higher-order Bragg peaks from the attenuation for the fundamental energy, thereby correcting for the harmonic contamination to the fundamental measurement. Harmonic effects up to 15% at energies lower than 7 keV were observed with two foils (10 µm and 12 µm).

This is the highest level of harmonic correction thus far achieved through applying this method.

4.2. Roughness correction

Attenuation of the 10 µm foil was affected by roughness, which was clear from the residual signature of the foil.

The roughness r.m.s. of the 10 µm foil was found to be 1.1 µm for the energy range 7–17 keV, for which the mass attenuation coefficient of the foil was corrected (Glover *et al.*, 2008).

4.3. Effects of fluorescence

The interaction between X-rays with energies higher than that of the silver L_1 edge and the silver samples can produce fluorescent photons. The present measurements were made in the 5–20 keV energy range which does not contain any absorption edge but the energies fall in between the L_1 and K edges which can produce fluorescent photons due to the X-rays with energies higher than the L_1 edge. The fraction of fluorescent photons scattered can be determined from aperture-dependent measurements (Glover *et al.*, 2008; de Jonge *et al.*, 2005). To observe the effect of scattering, each of the scattered intensities was recorded using two different-sized apertures located on the daisy wheels between the samples and ion chambers (Fig. 10).

As expected, away from absorption edges the fluorescence correction was almost negligible (0.025%) (Fig. 10).

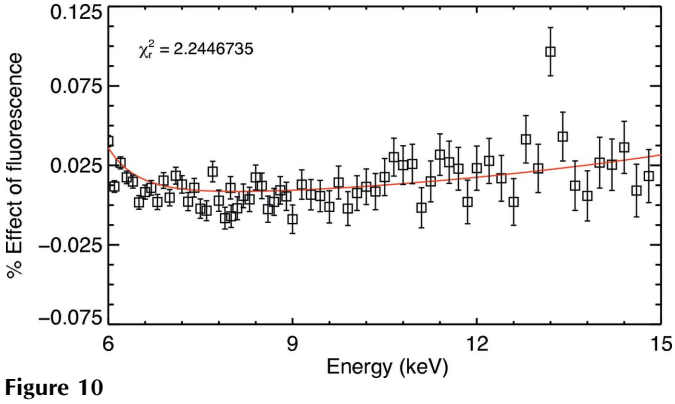

Figure 10
Effect of fluorescence on the measurements for the 12 µm-thick foil. A maximum of 0.025% fluorescence contribution was determined from the percentage difference in the measurements using two different-sized apertures.

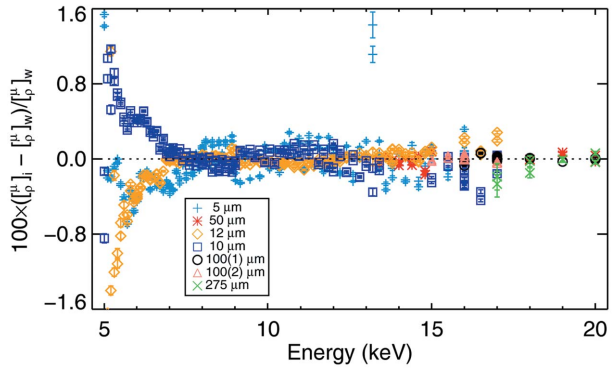

Figure 11
Consistency between the measurements for different foil thicknesses and aperture sizes. This represents the percentage difference between $[\mu/\rho]$ of the individual foil and aperture measurements and their weighted mean at each of the energies. The 10 µm- and 12 µm-thick foils showed relatively good consistency at energies lower than 5.6 keV and consistency with the thinnest foil (5 µm) was found to be excellent throughout the energy range of measurements. A 10–25% harmonic contamination was found at lower energies, <8 keV, and correction was made to attain good consistency. The thickest foil (12 µm) in this energy range was affected most by the harmonic content.

4.4. Aperture- and thickness-dependent consistency of the results

At each of the measured energies, multiple values of the X-ray mass attenuation coefficient $[\mu/\rho]$ of silver were obtained by the use of multiple thicknesses, and two different-sized apertures on the daisy wheels allowed aperture-dependent measurements. We tested the consistency of the obtained X-ray mass attenuation coefficients of silver using those multiple measurements at each of the energies. For this consistency test, the percentage variation between the weighted mean and individual values was investigated (Fig. 11).

Excellent consistency was achieved within 0.1% from 6 keV to 17 keV, with somewhat poorer consistency found below 6.5 keV and above 17 keV. The measurements below 6.5 keV contributed slightly larger uncertainties with the 10 µm and 12 µm foils, possibly due to incomplete subtraction of harmonic contributions. At the lowest two to three energies measured the influence of several systematics increases the variance and uncertainty.

4.5. Comparison of this work with theories and other experiments

The US National Institute for Standards and Technology (NIST) recommends two theoretical tabulations, FFAST (Chantler, 1995, 2000) and XCOM (Berger *et al.*, 1998; Saloman *et al.*, 1988), for the photoelectric absorption, and Compton and Rayleigh scattering of X-rays are commonly also used in the calculation of the X-ray mass attenuation coefficient. The measured X-ray mass attenuation coefficients of silver of this work are compared with the FFAST and XCOM tabulated values and found to be within 2% at the higher energies, with discrepancies increasing towards lower energies. The results were also compared with the few other

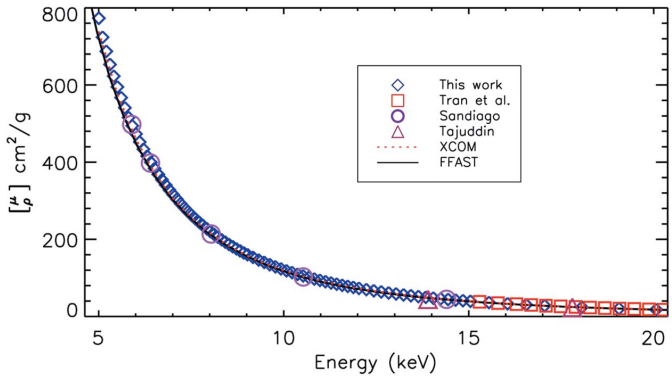

Figure 12
Comparison of this work with two theories and other experimental measurements. This work is represented by diamonds, Sandiago & Gowa (1997) by circles, Tajuddin *et al.* (1995) by triangles and Tran *et al.* (2005) by squares. Two theoretical values FFAST and XCOM are represented by solid and dotted lines. This conventional comparison does not provide information about the discrepancy between the measurements. The following plot of percentage difference of the measurements from the FFAST tabulated values reveals the discrepancy between the measurements and the theories (Fig. 13).

experimental measurements in the literature in this energy range (5–20 keV).

Our results (Figs. 12 and Fig. 13) show excellent agreement with the careful work of Tran *et al.* (2005) collected under independent conditions, with agreement to within one standard error across the range 16–20 keV, with a standard error of about 0.1%. The results also confirm a discrepancy with the FFAST tabulation of about 2% at the higher energies, which appears to increase towards lower energies. Comparison of the data with XCOM theory is smoother but also reaches 2%. This is not surprising since the theoretical predictions have an accuracy of order 1%.

This investigation calls for further investigations of the L_1 and K edges of silver using the XERT which is able to obtain

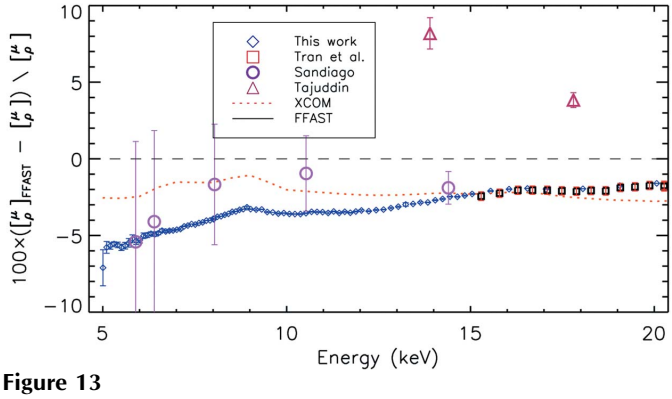

Figure 13
Percentage discrepancy between theories and other experimental measurements. This work shows excellent agreement with the careful work of Tran *et al.* (2005) collected under independent conditions, with agreement to within one standard error across the range from 16 keV to 20 keV for a standard error of about 0.1%. The results also confirm a discrepancy between the measurements and the FFAST tabulation of about 2% at the higher energies, which increases towards lower energies. Comparison of the data to XCOM theory shows better agreement but also reaches 3%. This is not surprising since the theoretical predictions have an accuracy of order 1%.

high accuracy in the energy ranges across the L_1 and K absorption edges.

5. Results and discussion

5.1. The mass attenuation coefficients of silver

The mass attenuation coefficients of silver metal foils were determined by the XERT approach and presented in Table 2. Six silver foils with different thicknesses were used in the energy range between 5 keV and 20 keV. To obtain the final attenuation coefficient $[\mu/\rho]$ at a given energy, the weighted mean of $[\mu/\rho]$ obtained from the different foil thicknesses and aperture-dependent measurements at that energy was used,

$$[\mu/\rho] = \sum_{\text{all}} [\mu/\rho]_i/\sigma^2_{[\mu/\rho]_i} \Big/ \sum_{\text{all}} 1/\sigma^2_{[\mu/\rho]_i}, \qquad (7)$$

where $[\mu/\rho]_i$ are the measured mass attenuation coefficients obtained from the different thicknesses and $\sigma_{[\mu/\rho]_i}$ are the corresponding errors of the measurements,

$$\sigma_{[\mu/\rho]} = \left[\frac{\sum_i \{([\mu/\rho]_i - \overline{[\mu/\rho]})/\sigma_{[\mu/\rho]_i}\}^2}{(N-1)\sum_i 1/\sigma^2_{[\mu/\rho]_i}} + \left(\frac{\sigma_{[\rho t]_c}}{[\rho t]_c}\right)^2 \right]^{1/2}, \qquad (8)$$

where $\overline{[\mu/\rho]}$ is the weighted average of the $[\mu/\rho]_i$, $\sigma_{[\mu/\rho]_i}$ are the corresponding statistical errors in $[\mu/\rho]_i$, and N is the number of foils with different thicknesses measured at a given energy.

The obtained mass attenuation coefficients using the integrated column densities $[\rho t]_c$ by central-foil mapping have been found to be consistent with the full-foil mapping to within 0.15%. A summary of uncertainty and error contributions is presented in Table 3.

5.2. Derivation of photoelectric absorption, form factor and scattering components

Theoretically tabulated (FFAST and XCOM) scattering cross sections $[\mu/\rho]_{R+C}$ were derived (by interpolation) for the measured experimental energies at which X-ray mass attenuation coefficients were determined. The photoelectric mass absorption coefficient $[\mu/\rho]_{pe}$ was then determined by subtracting the theoretically tabulated scattering cross sections $[\mu/\rho]_{R+C}$ from the measured total mass attenuation coefficients $[\mu/\rho]$ (Tran *et al.*, 2004). In this analysis, we used $[\mu/\rho]_{R+C}$ averaging the XCOM (Berger *et al.*, 1998; Saloman *et al.*, 1988) and FFAST (Chantler, 1995, 2000) tabulated values. The corresponding uncertainty of $[\mu/\rho]_{pe}$ was determined from the half of the variation between the two tabulations. The imaginary component of the atomic form factor f'' is directly related to the photoelectric absorption,

$$f'' = \frac{EuA[\mu/\rho]_{pe}}{2hcr_e}, \qquad (9)$$

where E is the photon energy in eV, u is the atomic mass unit, A is the relative atomic mass of silver, h is the Planck constant,

Table 2
Measured total X-ray mass attenuation coefficients $[\mu/\rho]_t$, photoelectric mass absorption coefficients $[\mu/\rho]_{pe}$, imaginary components of the form factor f'' and the mass attenuation coefficients for Raleigh and Compton scattering $[\mu/\rho]_{R+C}$ of silver in the 5–20 keV energy range, and their corresponding uncertainties..

The first column lists the measured energies (with uncertainties in eV) at which the quantities were determined. The second column lists the total mass attenuation coefficients with absolute uncertainties in parentheses. The third and fourth columns list the corresponding percentage relative and absolute uncertainties. The fifth column lists the photoelectric mass absorption coefficients determined by subtracting the mass attenuation coefficients for Rayleigh and Compton scattering from the total experimental absolute mass attenuation coefficients at the measured energies. The mass attenuation coefficients for Rayleigh and Compton scattering were taken as the average of FFAST and XCOM tabulated values and determined by interpolation at the measured energies. The uncertainty of $[\mu/\rho]_{R+C}$ was determined from half of the variation between FFAST and XCOM tabulated values. The uncertainty of $[\mu/\rho]_{pe}$ was determined from the uncertainty contributions of $[\mu/\rho]_{R+C}$ and $[\mu/\rho]_t$. The imaginary components of the form factor were determined using equation (9). The uncertainty in f'' was estimated using equation (10).

Energy (keV)	$[\mu/\rho]_t$ ($cm^2\ g^{-1}$)	$\sigma([\mu/\rho]_r)$ (% absolute)	$\sigma([\mu/\rho]_a)$ (% absolute)	$[\mu/\rho]_{pe}$ ($cm^2\ g^{-1}$)	f'' (e $atom^{-1}$)	$[\mu/\rho]_{R+C}$ ($cm^2\ g^{-1}$)
20.06525 (58)	17.9785 (20)	0.011	0.088	16.740 (11)	0.86101 (56)	1.239 (13)
19.06124 (52)	20.6921 (36)	0.017	0.089	19.373 (11)	0.94660 (55)	1.319 (14)
18.05718 (46)	24.0298 (14)	0.006	0.087	22.622 (11)	1.04711 (49)	1.408 (15)
17.05313 (41)	28.1240 (28)	0.010	0.088	26.617 (10)	1.16355 (44)	1.507 (15)
16.55110 (39)	30.499 (22)	0.071	0.113	28.939 (24)	1.2278 (10)	1.561 (15)
16.04910 (36)	33.1993 (81)	0.024	0.090	31.582 (12)	1.29929 (49)	1.618 (14)
15.54701 (34)	36.2281 (66)	0.018	0.089	34.551 (10)	1.37697 (41)	1.677 (13)
15.04497 (33)	39.659 (12)	0.030	0.092	37.918 (14)	1.46237 (53)	1.741 (12)
14.84420 (32)	41.164 (19)	0.046	0.098	39.396 (20)	1.49911 (76)	1.767 (12)
14.64342 (31)	42.755 (11)	0.025	0.090	40.960 (12)	1.53753 (46)	1.794 (11)
14.44257 (31)	44.3646 (80)	0.018	0.089	42.5425 (98)	1.57503 (36)	1.822 (10)
14.24172 (30)	46.135 (16)	0.035	0.094	44.284 (17)	1.61670 (62)	1.8516 (95)
14.04092 (30)	47.954 (12)	0.026	0.091	46.074 (13)	1.65834 (47)	1.8797 (86)
13.84015 (30)	49.9145 (96)	0.019	0.089	48.005 (10)	1.70313 (37)	1.9096 (77)
13.63934 (29)	51.919 (17)	0.032	0.093	49.979 (17)	1.74743 (59)	1.9401 (67)
13.43850 (29)	54.074 (10)	0.019	0.089	52.102 (11)	1.79485 (37)	1.9715 (55)
13.23773 (29)	56.285 (84)	0.149	0.172	54.281 (84)	1.8420 (28)	2.0036 (42)
13.03687 (29)	58.743 (16)	0.027	0.091	56.707 (16)	1.89509 (54)	2.0365 (28)
12.83611 (29)	61.291 (28)	0.045	0.098	59.221 (28)	1.94864 (91)	2.0701 (11)
12.63525 (29)	64.020 (24)	0.037	0.094	61.916 (24)	2.00543 (76)	2.10460 (63)
12.43446 (29)	66.873 (20)	0.030	0.092	64.733 (20)	2.06338 (65)	2.1400 (25)
12.23364 (29)	69.933 (20)	0.029	0.092	67.756 (21)	2.12485 (64)	2.1766 (44)
12.03285 (29)	73.152 (20)	0.027	0.091	70.938 (20)	2.18812 (61)	2.2141 (64)
11.88227 (29)	75.687 (23)	0.030	0.092	73.444 (23)	2.23709 (70)	2.2430 (79)
11.73163 (30)	78.409 (24)	0.031	0.092	76.136 (25)	2.28969 (74)	2.2725 (95)
11.58104 (30)	81.158 (25)	0.031	0.092	78.856 (26)	2.34102 (76)	2.303 (11)
11.43044 (30)	84.149 (36)	0.042	0.097	81.815 (36)	2.3973 (11)	2.333 (13)
11.27979 (31)	87.181 (24)	0.027	0.091	84.817 (25)	2.45250 (71)	2.365 (15)
11.12919 (31)	90.540 (46)	0.051	0.101	88.143 (46)	2.5147 (13)	2.397 (17)
10.97859 (31)	93.897 (22)	0.023	0.090	91.467 (23)	2.57418 (65)	2.429 (19)
10.82801 (32)	97.485 (41)	0.042	0.097	95.022 (42)	2.6375 (12)	2.463 (21)
10.67736 (32)	101.250 (25)	0.025	0.091	98.753 (27)	2.70296 (74)	2.497 (24)
10.52679 (33)	105.358 (21)	0.020	0.089	102.827 (23)	2.77478 (63)	2.532 (26)
10.37618 (33)	109.663 (39)	0.036	0.094	107.096 (41)	2.8486 (11)	2.568 (28)
10.22556 (34)	114.133 (15)	0.013	0.088	111.529 (19)	2.92348 (50)	2.604 (31)
10.07496 (35)	118.853 (37)	0.031	0.092	116.211 (39)	3.0014 (10)	2.642 (33)
9.92435 (35)	123.792 (21)	0.017	0.089	121.112 (25)	3.08118 (63)	2.681 (36)
9.77371 (36)	129.140 (42)	0.032	0.093	126.420 (44)	3.1674 (11)	2.720 (38)
9.62312 (36)	134.677 (08)	0.006	0.087	131.916 (17)	3.25420 (41)	2.761 (41)
9.47253 (37)	140.651 (58)	0.041	0.096	137.850 (60)	3.3474 (15)	2.802 (43)
9.32192 (38)	146.798 (32)	0.021	0.090	143.954 (36)	3.44001 (85)	2.844 (46)
9.17131 (38)	153.554 (64)	0.041	0.096	150.667 (66)	3.5423 (15)	2.888 (49)
9.02069 (39)	160.660 (32)	0.020	0.089	157.727 (37)	3.64736 (85)	2.932 (52)
8.92029 (40)	165.237 (96)	0.058	0.105	162.275 (98)	3.7107 (22)	2.963 (54)
8.81988 (40)	170.545 (23)	0.013	0.088	167.552 (30)	3.78828 (67)	2.994 (56)
8.71947 (41)	175.848 (58)	0.033	0.093	172.822 (61)	3.8630 (14)	3.025 (58)
8.61909 (41)	181.513 (18)	0.010	0.088	178.455 (27)	3.94296 (60)	3.057 (60)
8.51867 (42)	187.243 (68)	0.037	0.094	184.153 (71)	4.0215 (16)	3.090 (62)
8.41826 (42)	193.382 (24)	0.012	0.088	190.259 (31)	4.10582 (67)	3.123 (64)
8.31785 (43)	199.733 (76)	0.038	0.095	196.576 (79)	4.1916 (17)	3.157 (66)
8.21747 (43)	206.406 (13)	0.006	0.087	203.214 (25)	4.28080 (52)	3.192 (68)
8.11704 (44)	213.266 (69)	0.032	0.093	210.039 (73)	4.3705 (15)	3.227 (70)
8.01663 (44)	220.693 (33)	0.015	0.088	217.430 (40)	4.46835 (82)	3.263 (72)
8.00711 (44)	221.235 (56)	0.025	0.091	217.969 (60)	4.4741 (12)	3.266 (72)
7.91623 (45)	228.262 (21)	0.009	0.088	224.963 (31)	4.56525 (63)	3.299 (74)

c is the speed of light and r_e is the classical electron radius. The corresponding uncertainty in f'' was evaluated using

$$\sigma_{f''} = \frac{EuA}{2hcr_e}\left(\sigma^2_{[\mu/\rho]} + \Delta^2_{RC}\right)^{1/2}. \quad (10)$$

5.3. Independent verification of potential accuracy of XERT

Comparison of results reported here with an earlier data set optimized for higher energies (Tran *et al.*, 2005) confirms agreement to within one standard error of each data set collected and analysed using the principles of the XERT, in the region over which they overlap. These results (Figs. 12 and 13) show excellent agreement with the careful earlier work (Tran *et al.*, 2005) collected under independent conditions, with agreement to within one standard error across the range 16 keV to 20 keV, with a standard error of about 0.1%.

The earlier work reported accuracies between 0.27% and 0.4% away from the *K*-edge from measurements at the Advanced Photon Source, Chicago, 1BM, using a silicon 400 monochromating diffracting crystal, 2 mm × 2 mm aperture and N_2 in ion chambers. The current data were collected at beamline 20B of the Photon Factory in Tsukuba, Japan. The X-ray beam was monochromated by a double-crystal monochromator using a monolithic silicon 111 crystal located in the first optical enclosure. The monochromated X-rays were passed through a pair of orthogonal adjustable slits for defining the beam cross section (approximately 2 mm × 1.5 mm). Harmonics, collimation, monochromatic and energy range were different in the two experiments. The sample stage location was also different, implying that systematic corrections including scattering were also of a different magnitude. While some of the foils used as samples were the same, the principle foil thicknesses used in the experiment were different. Even when the same

Table 2 (continued)

Energy (keV)	$[\mu/\rho]_t$ ($cm^2\ g^{-1}$)	$\sigma([\mu/\rho]_r)$ (% absolute)	$\sigma([\mu/\rho]_a)$ (% absolute)	$[\mu/\rho]_{pe}$ ($cm^2\ g^{-1}$)	f'' (e $atom^{-1}$)	$[\mu/\rho]_{R+C}$ ($cm^2\ g^{-1}$)
7.81584 (45)	236.089 (35)	0.015	0.088	232.752 (42)	4.66342 (84)	3.336 (76)
7.71542 (46)	244.576 (56)	0.023	0.090	241.202 (61)	4.7706 (12)	3.374 (78)
7.61504 (46)	253.292 (29)	0.012	0.088	249.879 (38)	4.87796 (73)	3.413 (80)
7.51462 (47)	262.520 (80)	0.031	0.092	259.068 (84)	4.9907 (16)	3.452 (82)
7.41422 (47)	271.873 (18)	0.006	0.087	268.381 (30)	5.10099 (57)	3.492 (84)
7.31381 (48)	282.11 (11)	0.040	0.096	278.57 (12)	5.2230 (22)	3.533 (86)
7.21342 (48)	292.731 (69)	0.024	0.090	289.156 (74)	5.3470 (14)	3.575 (88)
7.11301 (49)	304.17 (19)	0.065	0.108	300.55 (20)	5.4804 (36)	3.617 (90)
7.01258 (50)	316.101 (95)	0.030	0.092	312.440 (98)	5.6167 (18)	3.661 (92)
6.91218 (50)	328.37 (12)	0.036	0.094	324.67 (12)	5.7530 (22)	3.705 (94)
6.81178 (51)	341.17 (29)	0.084	0.121	337.42 (29)	5.8921 (50)	3.750 (96)
6.71138 (51)	354.71 (26)	0.072	0.113	350.91 (26)	6.0374 (44)	3.796 (98)
6.61096 (52)	368.63 (37)	0.101	0.134	364.79 (38)	6.1823 (64)	3.84 (10)
6.51058 (52)	383.96 (36)	0.095	0.129	380.07 (37)	6.3434 (61)	3.89 (10)
6.41016 (53)	400.29 (46)	0.114	0.143	396.34 (46)	6.5130 (75)	3.94 (10)
6.30977 (54)	416.86 (47)	0.112	0.142	412.87 (47)	6.6784 (76)	3.99 (11)
6.20935 (54)	434.79 (58)	0.133	0.159	430.75 (58)	6.8568 (92)	4.04 (11)
6.10894 (55)	454.13 (69)	0.151	0.174	450.04 (69)	7.047 (11)	4.09 (11)
6.00853 (55)	474.92 (59)	0.124	0.151	470.78 (59)	7.2515 (91)	4.14 (11)
5.90815 (56)	496.93 (97)	0.195	0.214	492.73 (97)	7.463 (15)	4.20 (11)
5.80774 (57)	518.90 (95)	0.183	0.203	514.64 (95)	7.662 (14)	4.25 (11)
5.70733 (57)	545 (1)	0.199	0.217	540 (1)	7.904 (16)	4.31 (11)
5.60692 (58)	569 (1)	0.194	0.212	565 (1)	8.120 (16)	4.37 (11)
5.50652 (58)	595 (1)	0.215	0.232	591 (1)	8.339 (18)	4.43 (11)
5.40611 (59)	623 (1)	0.175	0.196	618 (1)	8.566 (15)	4.49 (11)
5.30571 (60)	654 (1)	0.207	0.225	649 (1)	8.831 (18)	4.55 (12)
5.20530 (60)	687 (2)	0.273	0.286	682 (2)	9.107 (25)	4.61 (12)
5.10490 (61)	722 (3)	0.420	0.428	717 (3)	9.387 (40)	4.67 (12)
5.00449 (61)	746 (9)	1.217	1.220	741 (9)	9.50 (12)	4.73 (12)

Table 3
Error contributions from variance and experimental systematics to 5.1 keV.

Quantity	Estimated errors	Uncertainty contributions
$[\mu/\rho]$	0.005–0.181%	Relative uncertainty from variance
	0.0025%	Fluorescence scattering
	0.001–0.002%	Harmonic contaminations
	0.01–0.4%	Weighted average of multiple samples at the same energy and roughness
$[\mu/\rho][\rho t]_c$	0.048%	Integrated column density determination and X-ray raster scan
E	0.3–0.6 eV	Energy calibration

foils were used, the points on the foil through which the X-ray beam passed were not the same.

Interestingly, both experiments used powder diffraction to calibrate the energies of the measured attenuations; but whereas the earlier experiment used a single Si 640b standard powder on a scanning six-circle goniometer, the current experiment used the powder in an image-plate environment using BigDiff, the large Australian powder diffractometer. The systematics for each of these differences are independent and the agreement from such different beamlines and arrangements is therefore quite remarkable.

The key marker for the self-consistency of the data after removal of systematic contributions is Fig. 10 of the earlier publication compared with Fig. 11 of this current paper. The consistencies are very similar, and it is not clear which results are superior on that basis. In the tables, the earlier experiment separated the statistical precision from the absolute measurement, and noted that the dominant systematic was the absolute calibration of the foils, with the second most dominant being the statistical precision, especially at the high energies involved.

Conversely, in the current experiment, the precision is generally improved, and the relative accuracy is generally improved; a significant uncertainty arises from the absolute calibration of the primary foil, and a significant uncertainty arises from the variance between measurements of different foils, including the accuracy of the transfer of thickness determination from primary foils to secondary foils (at higher energies). The fact that so many variables were so different and yet the overall technique generated accurate and consistent results in the region of overlap, at the extremes of energy of both data sets, is perhaps the greatest achievement of the X-ray extended range technique.

6. Conclusion

The X-ray mass attenuation coefficients of silver were determined with an accuracy of 0.01–0.2% on a relative scale down to 5.3 keV, and of 0.09–1.22% on an absolute scale to 5.0 keV. This analysis provides the most accurate measured X-ray mass attenuation coefficients of silver in the 5–20 keV energy range. The methodology developed in this analysis will be important for the XAFS investigation of the L and K edges of silver.

One of the key achievements from this analysis is the attainment of high accuracy at lower energies (lower than 10 keV) for such a high-Z element. This analysis indicates that high accuracy is obtainable at lower energies by the use of comparatively thin foils (5 µm) and by the use of dilute solutions of silver compounds if accurate transfer is possible. This work thus indicates that measurements of L-edge XAFS of silver (theoretically at 3.8 keV) are possible using XERT by making use of thinner silver foils at lower energies (3–6 keV).

Perhaps just as significant is the independent verification of the accuracy of the earlier work of Tran *et al.* (2005) to within one standard error, which confirms the potential accuracy of this technique and the portability with different diffracting monochromator crystals, energy ranges and foils.

The Australian Research Council (ARC) and the science faculty of the University of Melbourne are acknowledged for funding this work. The authors would like to thank the staff of

the Australian National Beamline Facility (ANBF), Tsukuba, Japan, where the experiment was performed for their assistance in this work. As the ANBF is now closed, we dedicate this work to the efforts of the Australian and Japanese scientists who have worked together to make the beamline and collaboration such a success.

References

Barnea, Z. & Mohyla, J. (1974). *J. Appl. Cryst.* **7**, 298–299.

Berger, M. J., Hubbell, J. H., Seltzer, S. M., Chang, J., Coursey, J. S., Sukumar, R. & Zucker, D. S. (1998). *NIST Stand. Ref. Database*, **8**, 87–3597.

Chantler, C. T. (1995). *J. Phys. Chem. Ref. Data*, **24**, 71–82.

Chantler, C. T. (2000). *J. Phys. Chem. Ref. Data*, **29**, 597–1048.

Chantler, C. T. (2009). *Eur. Phys. J.* **169**, 147–153.

Chantler, C. T., Rae, N. A., Islam, M. T., Best, S. P., Yeo, J., Smale, L. F., Hester, J., Mohammadi, N. & Wang, F. (2012). *J. Synchrotron Rad.* **19**, 145–158.

Chantler, C. T., Tran, C. Q., Paterson, D. & Barnea, Z. (2001). *Phys. Lett. A*, **286**, 338–346.

Gerward, L. (1989). *Acta Cryst.* A**45**, 1–3.

Gerward, L., Thuesen, G., Stibius Jensen, M. & Alstrup, I. (1979). *Acta Cryst.* A**35**, 852–857.

Glover, J. L. & Chantler, C. T. (2007). *Meas. Sci. Technol.* **18**, 2916–2920.

Glover, J. L., Chantler, C. T., Barnea, Z., Rae, N. A., Creagh, D. C., Paterson, D. & Dhal, B. B. (2008). *Phys. Rev. A*, **78**, 052902.

Glover, J. L., Chantler, C. T., Barnea, Z., Rae, N. A. & Tran, C. Q. (2010). *J. Phys. B*, **43**, 085001.

Glover, J. L., Chantler, C. T. & de Jonge, M. D. (2009). *Phys. Lett. A*, **373**, 1177–1180.

Han, S. W., Stern, E. A., Haskel, D. & Moodenbaugh, A. R. (2002). *Phys. Rev. B*, **66**, 094101.

Hopersky, A. N., Petrov, I. D., Nadolinsky, A. M., Yavna, V. A. & Koneev, R. V. (2004). *J. Phys. B*, **37**, 3313–3320.

Hossain, F., Riley, D. & Murch, G. (2005). *Phys. Rev. B*, **72**, 235101.

Ignatov, A., Yu, Ali, N. & Khalid, S. (2001). *Phys. Rev. B*, **64**, 014413.

Islam, M. T., Rae, N. A., Glover, J. L., Barnea, Z., de Jonge, M. D., Tran, C. Q., Wang, J. & Chantler, C. T. (2010). *Phys. Rev. A*, **81**, 022903.

Joly, Y. (2001). *J. Phys. B*, **63**, 125120.

Jonge, M. D. de, Barnea, Z., Tran, C. Q. & Chantler, C. T. (2004*a*). *Phys. Rev. A*, **69**, 022717.

Jonge, M. D. de, Tran, C. Q., Chantler, C. T. & Barnea, Z. (2006). *Opt. Eng.* **45**, 046501.

Jonge, M. D. de, Tran, C. Q., Chantler, C. T., Barnea, Z., Dhal, B. B., Cookson, D. J., Lee, W. K. & Mashayekhi, A. (2004*b*). *Meas. Sci. Technol.* **15**, 1811–1822.

Jonge, M. D. de, Tran, C. Q., Chantler, C. T., Barnea, Z., Dhal, B. B., Cookson, D. J., Lee, W. K. & Mashayekhi, A. (2005). *Phys. Rev. A*, **71**, 032702.

Karabulut, A., Gurol, A., Budak, G. & Ertugrul, M. (2005). *Nucl. Instrum. Methods Phys. Res. B*, **227**, 485–489.

Khoperskii, A., Nadolinskii, A., Yavna, V. & Koneev, R. (2005). *Opt. Spectrosc.* **98**, 161–165.

Lee, M. J., Hahn, P. F., Papanicolaou, N., Egglin, T. K., Saini, P. R., Mueller, S. & Simeone, J. F. (1991). *Radiology*, **179**, 415–418.

Lytle, F. (2007). *Synchrotron Radiat. News*, **20**, 9.

Machali, F., Al-Barakati, G. G., El-Sayed, A. A. & Altaf, W. J. (1987). *J. Phys. F*, **17**, 1279–1284.

Mica, J. F., Martin, L. J. & Barnea, Z. (1985). *J. Phys. C*, **18**, 5215–5223.

Pettifer, R. F., Borowski, M. & Loeffen, P. W. (1999). *J. Synchrotron Rad.* **6**, 217–219.

Rae, N. A., Chantler, C. T., Barnea, Z., de Jonge, M. D., Tran, C. Q. & Hester, J. R. (2010). *Phys. Rev. A*, **81**, 022904.

Rae, N. A., Chantler, C. T., Tran, C. Q. & Barnea, Z. (2006). *Radiat. Phys. Chem.* **75**, 2063–2066.

Rehr, J. & Albers, R. (2000). *Rev. Mod. Phys.* **72**, 621–654.

Saloman, E. B., Hubbell, J. H. & Scofield, J. H. (1988). *At. Data Nucl. Data Tables*, **38**, 1.

Sandiago, T. K. U. & Gowa, R. (1997). *Pramana*, **48**, 1077.

Tajuddin, A. A., Chong, C., Shukri, A., Bandyopadhyay, T. & Bradley, A. (1995). *Appl. Radiat. Isot.* **46**, 113–115.

Tantau, L. J., Islam, M. T., Payne, A. T., Tran, C. Q., Cheah, M. H., Best, S. P. & Chantler, C. T. (2013). *Radiat. Phys. Chem.* In the press.

Tran, C. Q., Barnea, Z., de Jonge, M. D., Dhal, B. B., Paterson, D., Cookson, D. J. & Chantler, C. T. (2003*a*). *X-ray Spectrom.* **32**, 69–74.

Tran, C. Q., Chantler, C. T. & Barnea, Z. (2003*b*). *Phys. Rev. Lett.* **90**, 257401.

Tran, C. Q., Chantler, C. T., Barnea, Z., de Jonge, M. D., Dhal, B. B., Chung, C. T. Y., Paterson, D. & Wang, J. (2005). *J. Phys. B*, **38**, 89–107.

Tran, C. Q., Chantler, C. T., Barnea, Z., Paterson, D., Cookson, D. J. & Balaic, D. X. (2003*c*). *Phys. Rev. A*, **67**, 042716.

Tran, C. Q., de Jonge, M. D., Barnea, Z. & Chantler, C. T. (2004). *J. Phys. B*, **37**, 3163–3176.